

Engineering Anisotropic Rabi Model in Circuit QED

S. Mojtaba Tabatabaei,¹ Babak Zare Rameshti,² and Mohsen Akbari¹

¹*Department of Physics, Kharazmi University, Tehran, Iran*

²*Department of Physics, Iran University of Science and Technology, Narmak, Tehran 16844, Iran*

The anisotropic Rabi model (ARM), which features tunable Jaynes-Cummings (JC) and anti-Jaynes-Cummings (AJC) interactions, has remained challenging to realize fully. We present a circuit QED implementation that provides static control over the ARM parameters. By simultaneously coupling a qubit to a resonator's voltage and current antinodes, we geometrically tune the interaction from pure JC to pure AJC. This control enables novel quantum measurement capabilities, including dispersive shift cancellation and Purcell-suppressed readout. Our work establishes a direct platform for exploring the ARM's full parameter space and its applications in quantum information processing.

I. INTRODUCTION

The ability to coherently couple artificial atoms to quantized electromagnetic modes underlies many of the key developments in quantum electronics, from fundamental studies of light-matter interaction to the implementation of superconducting quantum processors. In circuit quantum electrodynamics (circuit QED), this interaction can be engineered with unprecedented precision by integrating superconducting qubits with on-chip microwave resonators, enabling strong and even ultrastrong coupling regimes that go far beyond the reach of conventional cavity QED [1, 2]. A typical platform in circuit-QED consists of a superconducting qubit coupled either capacitively or inductively to a superconducting coplanar waveguide (CPW) resonator [3, 4]. The underlying light-matter interaction between the cavity mode and the qubit is described by the Rabi model which is one of the most fundamental models of light-matter interaction in quantum physics [5]. This model comprises two distinct types of interactions: a resonant part $\propto (a^\dagger \sigma_- + a \sigma_+)$, that conserves the total number of excitations, and a counter-rotating part $\propto (a^\dagger \sigma_+ + a \sigma_-)$, that does not.

The counter-rotating part can be omitted using the rotating-wave approximation (RWA), when the cavity and qubit frequencies are near resonance and the coupling is not too strong. The RWA simplifies the Rabi model to the Jaynes-Cummings (JC) model which works well in the weak and strong coupling regimes of cavity and circuit QED [6]. The JC model has been the basic model to describe seminal demonstrations such as quantum non-demolition qubit readout [3], the generation of Fock states [7], the observation of multiphoton resonances [8], and the cavity mediated coupling between two qubits [9, 10].

However, the RWA breaks down in the ultra-strong [11] and deep-strong [12] coupling regimes, where the coupling strength becomes comparable to the system frequencies, as well as in the strong driving regimes [13, 14]. In these regimes, the counter rotating, or equivalently anti-Jaynes-Cummings (AJC) terms must be retained in the interaction Hamiltonian. The excitation-number nonconserving nature of these terms leads to nontrivial

phenomena absent in the JC model. These include modified energy spectra observed as Bloch-Siegert shifts [15–17], generation of Schrödinger cat states [18], asymmetries in vacuum Rabi splitting [19], multiphoton resonances [20], modified input-output relations [21], quantum phase transitions [22], and deterioration of photon blockade effects [23, 24]. Beyond static effects, the combination of JC and AJC terms in the Rabi model influences fundamental quantum effects such as the quantum Zeno effect [25] and entanglement evolution [26, 27], and plays a significant role in the dynamics of driven two-level systems [28, 29].

These non-RWA effects have been observed in various strongly driven systems [30–33] and have been leveraged for applications such as ultrafast, high-fidelity geometric quantum gates robust against decoherence [34]. Furthermore, parametric modulation of qubit-cavity coupling has been used to engineer both red-sideband (JC-like) [35–37] and blue-sideband (AJC-like) interactions [38–41], with the latter acting as a coherent two-photon pump. Emulation of these models in systems like modulated qutrits [42] and the demonstration of pure AJC effects in dipole-dipole coupling [43] further highlight the broad relevance of these interactions. Recent studies show that the AJC model with squeezed light exhibits distinct photon statistics and enhanced entanglement [44], while switching between JC and AJC dynamics can control quantum revivals [45].

A crucial observation is that all these phenomena result from the combined action of both JC and AJC interaction channels. In conventional circuit QED architectures with purely capacitive or inductive coupling, the AJC terms remain inherently weak compared to the dominant JC channel under the RWA. While parametric modulation can selectively enhance one channel, it requires external driving and operates effectively only when modulated at specific frequencies. This raises a fundamental question: is it possible to statically engineer the bare light-matter interaction itself—without time-dependent modulation—to cleanly isolate or balance these fundamental interaction channels?

In this work, we propose a simple yet powerful circuit that provides the answer. By placing a qubit in the

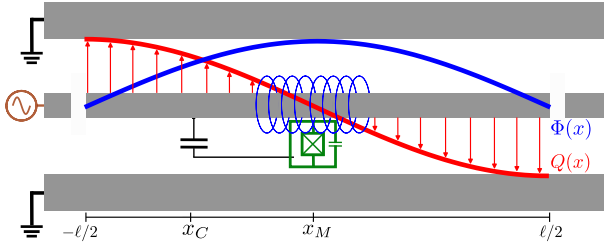


Figure 1. Schematic of the proposed circuit. A superconducting qubit (green) coupled simultaneously to a CPW resonator with length ℓ via a capacitive coupling C_g and an inductive coupling M . The spatial profiles of the fundamental mode of the resonator are also shown: flux $\Phi(x) \propto \sin(\pi x/\ell)$ (blue) and charge $Q(x) \propto \cos(\pi x/\ell)$ (red) standing waves. By tuning the positions x_C and x_M , the strength of both capacitive and inductive couplings and their relative sign can be controlled, enabling access to different regimes of the ARM.

vicinity of a coplanar waveguide resonator such that it couples simultaneously to the resonator's voltage antinode (capacitively) and current antinode (inductively), the JC and AJC amplitudes arise naturally with a tunable relative weight and phase. This platform enables the on-demand, static realization of both the pure JC and the pure AJC model within a single device. Crucially, it allows access to the pure JC interaction without making the conventional RWA, even in the ultra-strong and deep-strong coupling regimes, and to the pure AJC interaction without the need for external modulation. This provides a device-level mechanism to explore the distinct physics of each interaction channel, and opens new possibilities for symmetry-controlled quantum phases [46] and novel quantum information protocols. Furthermore, by providing independent control over both interaction channels, our scheme naturally realizes the anisotropic Rabi model (ARM) [47, 48], offering a versatile platform for exploring its full parameter space.

This manuscript is organized as follows. In Sec. II, we present the physical model and derive the effective qubit-resonator Hamiltonian. In Sec. III we analyze the system dynamics across the JC, Rabi, and AJC coupling regimes, focusing on transmission spectra, dispersive readout, and Purcell decay. In Sec. IV, we discuss the practical feasibility of implementing the proposed architecture using current superconducting circuit technology. Finally, Sec. V concludes the work with a summary of the main results and possible future directions.

II. PHYSICAL MODEL

A schematic of the proposed circuit is shown in Fig. 1. The qubit is placed in the vicinity of a CPW resonator such that it is coupled both to the resonator voltage antinode through a coupling capacitor C_g and to the resonator current antinode via a mutual inductance M . The inductive element can be realized using a shared segment

of superconducting wire or a designed coupling loop, and the capacitive path is formed by a coupling pad adjacent to the resonator. The simultaneous capacitive and inductive connection ensures that the qubit couples to both the resonator's electric and magnetic fields. The ratio of capacitive to inductive coupling strengths can be tuned through the circuit geometry, allowing independent control over the two interaction channels. The resonator itself may be a $\lambda/4$ or $\lambda/2$ CPW, though the concept is applicable as well to lumped-element resonators.

The total Hamiltonian of the circuit is given by (see Appendix A for the detailed derivation)

$$H_{\text{sys}} = H_{\text{res}} + H_{\text{qubit}} + H_C + H_M. \quad (1)$$

The resonator and qubit Hamiltonians are given by $H_{\text{res}} = \omega_r a^\dagger a$ and $H_{\text{qubit}} = -\frac{\omega_q}{2} \sigma_z$, respectively, where ω_r denotes the fundamental mode frequency of resonator, with a being the photon annihilation operator, and ω_q represents the qubit's excitation energy, with σ_z the Pauli-Z operator.

The capacitive interaction H_C originates from a coupling capacitance C_c between the qubit and the resonator. At the circuit level, this term modifies the qubit charging energy, leading to an interaction Hamiltonian proportional to the product of the qubit charge operator \hat{n} and the resonator voltage operator \hat{V}_r (see Appendix A). In the two-level approximation, the qubit charge operator \hat{n} maps to σ_y , while the resonator field is expressed in terms of photon creation and annihilation operators, $i(a^\dagger - a)$. The resulting interaction takes the form

$$H_C = ig_C (a - a^\dagger) \sigma_y, \quad (2)$$

with g_C being the capacitive coupling strength. Transforming into the interaction picture with respect to the bare qubit and resonator Hamiltonians yields terms oscillating at $\pm(\omega_q - \omega_r)$ and $\pm(\omega_q + \omega_r)$. Under the RWA, the rapidly oscillating counter-rotating contributions are neglected, leaving the standard JC interaction $H_C^{\text{RWA}} = g_C (a\sigma_+ + a^\dagger\sigma_-)$.

Inductive coupling arises when the qubit shares a mutual inductance M with the resonator current. At the Hamiltonian level, this interaction is proportional to the product of the qubit flux operator $\hat{\varphi}$ and the resonator current operator \hat{I}_r . In the two-level approximation of the qubit, the qubit flux operator maps to σ_x , while the resonator current is proportional to $(a^\dagger + a)$. The interaction Hamiltonian then takes the form

$$H_L = g_L (a + a^\dagger) \sigma_x, \quad (3)$$

where g_L denotes the inductive coupling strength. Similar to the capacitive case, moving to the interaction picture reveals both resonant and counter-rotating terms. Applying the RWA leaves the same JC form $H_L^{\text{RWA}} = g_L (a\sigma_+ + a^\dagger\sigma_-)$.

The coupling strengths g_C and g_L are not independent parameters but are determined by the qubit's position

relative to the resonator's spatial mode profile. For a $\lambda/2$ resonator of length ℓ , the fundamental mode's flux and charge standing waves are described by $f_r(x) \propto \sin(\pi x/\ell)$ and $\partial_x f_r(x) \propto \cos(\pi x/\ell)$, respectively. The capacitive coupling strength g_C is proportional to the charge polarity at the coupling point x_C , while the inductive coupling strength g_L is proportional to the flux amplitude at the inductive coupling point x_M . By placing the qubit's capacitive pad at a charge polarity antinode (e.g., $x_C = -\ell/2$) and its inductive coupling point at a flux antinode (e.g., $x_M = 0$), both couplings can be maximized. Moreover, since the charge polarity reverses at the two ends of the resonator, moving the capacitive coupling point from $x_C = -\ell/2$ to $x_C = \ell/2$ reverses the sign of g_C . Consequently, the relative sign between g_C and g_L can be engineered by tuning the coupling points x_C and x_M .

While either of the capacitive or the inductive couplings leads to an effective JC interaction Hamiltonian, their simultaneous presence is more interesting. In this case, the full interaction Hamiltonian $H_{\text{int}} = H_C + H_L$ can be decomposed into resonant and counter-rotating contributions,

$$H_{\text{int}} = g_{\text{JC}} (a^\dagger \sigma_- + a \sigma_+) + g_{\text{AJC}} (a^\dagger \sigma_+ + a \sigma_-), \quad (4)$$

where, the effective JC and AJC couplings are $g_{\text{JC}} = g_C + g_L$, and $g_{\text{AJC}} = g_C - g_L$. It is seen that by controlling the ratio g_L/g_C , the two coupling channels can interfere, allowing one to enhance or suppress either JC or AJC interaction channels. This is precisely enabled by the spatial dependence of the resonator's modes, as described above.

For later convenience, we define the total coupling strength as $g = \sqrt{g_{\text{JC}}^2 + g_{\text{AJC}}^2}$ and the mixing angle $\theta = \arctan(g_{\text{AJC}}/g_{\text{JC}})$. Thus, the geometric ratio $g_{\text{AJC}}/g_{\text{JC}}$ sets the mixing angle θ , providing direct experimental control over the anisotropy. Using this notation, Eq. (4) can be recast into the anisotropic Rabi model given by

$$H_{\text{int}} = g \cos \theta (a^\dagger \sigma_- + a \sigma_+) + g \sin \theta (a^\dagger \sigma_+ + a \sigma_-). \quad (5)$$

This highlights the tunability of the model. For instance, when $g_C = g_L$, we get $g_{\text{AJC}} = 0$ and thus $\theta = 0$, leading to a pure JC interaction Hamiltonian $H_{\text{int}}^{\text{JC}} = g (a^\dagger \sigma_- + a \sigma_+)$. Conversely, for $g_L = -g_C$, we get $g_{\text{JC}} = 0$ and the mixing angle becomes $\theta = \pi/2$, resulting in a pure AJC interaction Hamiltonian $H_{\text{int}}^{\text{AJC}} = g (a^\dagger \sigma_+ + a \sigma_-)$. This removes the need for external modulation schemes to access counter-rotating processes.

III. COMPARISON BETWEEN RABI, JC AND AJC COUPLING REGIMES

In typical circuit QED experiments, the qubit is coupled to the resonator either purely capacitively or purely inductively. Both of these coupling mechanisms, mediate a Rabi interaction, where both JC and AJC channels can

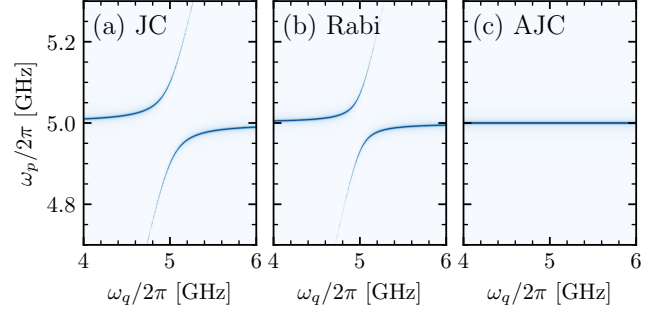


Figure 2. The resonator transmission is shown as a function of probe frequency ω_p and qubit frequency ω_q , for fixed coupling strengths. (a) JC regime ($\theta = 0$), (b) Rabi regime ($\theta = \pi/4$) and (c) AJC regime ($\theta = \pi/2$). Parameters are $\omega_r/2\pi = 5$ GHz, $\kappa = 1$ MHz, and $g/2\pi = 100$ MHz.

contribute depending on the experimental parameters in use. Indeed, in typical experiments the JC channel dominates, while the AJC terms remain weak and become relevant only in the ultrastrong-coupling or deep-strong coupling regimes. As we explained in the previous section, the proposed simultaneous capacitive and inductive coupling between the qubit and the resonator allows pure JC and pure AJC interactions to arise at the Hamiltonian level. It is thus useful to study how the dynamics of the coupled system will change depending on the precise coupling regime.

We first consider the transmission spectrum through the resonator in response to a weak probe field at frequency ω_p . The total Hamiltonian in this case becomes

$$H(t) = H_{\text{sys}} + 2\mathcal{E}_p (a + a^\dagger) \cos(\omega_p t), \quad (6)$$

where \mathcal{E}_p is the small amplitude for the probe field, and H_{sys} is given in Eq. (1). Now, by introducing the possible dissipation of the resonator and the qubit, the dynamics of this system is obtained by solving the Lindblad master equation

$$\frac{d\rho}{dt} = -i[H(t), \rho] + \kappa \mathcal{D}[a]\rho + \gamma \mathcal{D}[\sigma_-]\rho, \quad (7)$$

where κ is the cavity decay rate, γ is the qubit relaxation rate and the dissipator is defined as $\mathcal{D}[O]\rho = O\rho O^\dagger - \frac{1}{2}\{O^\dagger O, \rho\}$.

Figure 2(a-c), compares the transmission spectra in the JC ($\theta = 0$), Rabi ($\theta = \pi/4$) and AJC ($\theta = \pi/2$) regimes, respectively [49–51]. In the JC and Rabi cases, panels (a) and (b), a characteristic vacuum Rabi splitting can be observed when $\omega_q \approx \omega_r$. The splitting for the JC and Rabi cases at $\omega_q = \omega_r$ are given by $2g$ and $2g/\sqrt{2}$, respectively. This splitting reflects coherent Rabi oscillations between the states $|g, 1\rangle$ and $|e, 0\rangle$. By contrast, in the AJC regime, panel (c), no such splitting occurs.

This distinction can be understood by moving to a rotating frame. For the JC and Rabi Hamiltonians, applying the RWA results in a resonant JC-like interaction when $\omega_p \approx \omega_r \approx \omega_q$, with coupling strength g and

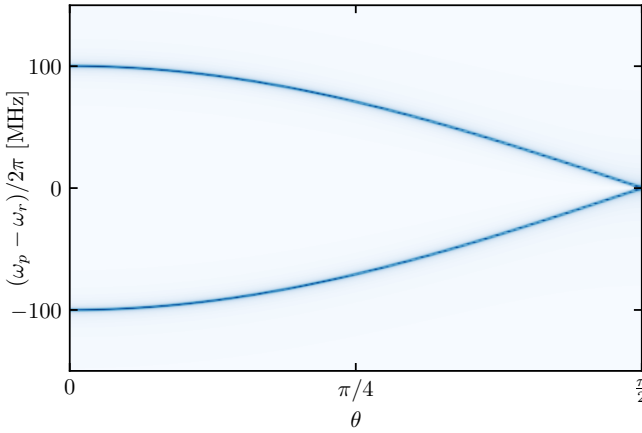


Figure 3. Evolution of the vacuum Rabi splitting with the coupling mixing angle θ . The plot shows the resonator transmission as a function of the probe frequency ω_p and the mixing angle θ , for a resonant qubit ($\omega_q = \omega_r$) and for constant coupling strength g . All parameters are as in Fig. 2.

$g/\sqrt{2}$, respectively. The interaction couples states $|g, 1\rangle$ and $|e, 0\rangle$, and leads to a vacuum Rabi splitting manifesting as the avoided crossing in the transmission spectrum which is seen in Figs. 2(a) and (b). On the other hand, in Fig. 2(c) with $\theta = \pi/2$ corresponding to the AJC regime, the interaction couples states $|g, 0\rangle$ and $|e, 1\rangle$, which are separated by a large energy $\omega_q + \omega_r$. This far-off-resonant interaction does not cause level repulsion at $\omega_q \approx \omega_r$, hence no splitting is observed in the spectrum.

The tunability of the model system is further illustrated in Fig. 3, which shows the resonator transmission as a function of both the probe frequency ω_p and the coupling mixing angle θ , with the qubit held fixed at resonance, $\omega_q = \omega_r$. At $\theta = 0$, corresponding to the pure JC regime, the spectrum exhibits a pronounced vacuum Rabi splitting of magnitude $2g$, consistent with the analysis of Fig. 2(a). As θ deviates from zero, the magnitude of the effective JC coupling $g_{\text{JC}} = g \cos \theta$ decreases. This causes the two peaks of the splitting to move symmetrically inward towards the central frequency $\omega_p = \omega_r$. The splitting continuously narrows, reaching a width of $2g/\sqrt{2}$ at $\theta = \pi/4$, which corresponds to the Rabi model with purely capacitive ($g_L = 0$) or purely inductive ($g_C = 0$) coupling. As θ increases further towards $\pi/2$ (the pure AJC regime), the effective JC coupling g_{JC} vanishes. Consequently, the splitting collapses entirely into a single Lorentzian peak at $\omega_p = \omega_r$, yielding the featureless single-peak spectrum seen in Fig. 2(c). This continuous evolution directly demonstrates the static control over the light-matter interaction Hamiltonian afforded by the simultaneous capacitive-inductive coupling scheme. It also shows that the AJC interaction channel, while present, does not contribute to the linear vacuum Rabi splitting.

Having clarified the transmission properties in the res-

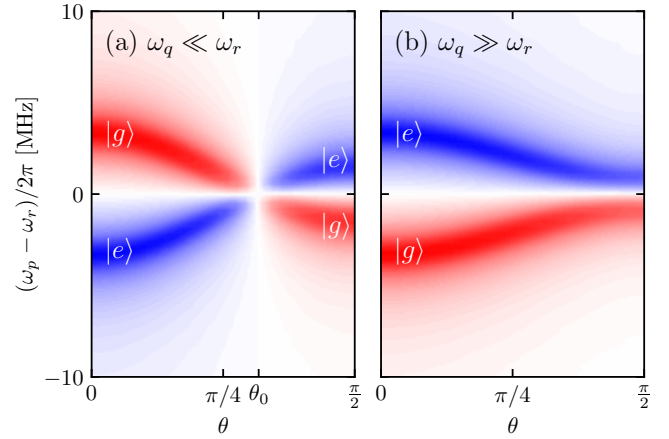


Figure 4. Dispersive readout of qubit across coupling regimes. The resonator transmission is shown as a function of probe frequency ω_p and mixing angle θ for the qubit prepared in its ground state $|g\rangle$ (red) and excited state $|e\rangle$ (blue). (a) With negative detuning $\omega_q \ll \omega_r$, the opposing signs of the JC and AJC dispersive shifts lead to a cancellation at a specific angle θ_0 , where the readout contrast vanishes. (b) For positive detuning $\omega_q \gg \omega_r$, the shifts do not cancel, and a finite readout contrast is maintained for all θ . The qubit frequency in (a) is $\omega_q/2\pi = 2$ GHz and in (b) is $\omega_q/2\pi = 8$ GHz. All other parameters are as in Fig. 2.

onant regime, we next turn to dispersive qubit readout, where the qubit frequency is largely detuned from the resonator. In this setting, the resonator's response to a probe depends on the qubit's state. The qubit's state dependent dispersive shifts of the resonator frequency χ in different coupling regimes can be derived via a Schrieffer-Wolff transformation [14] and are given by $\chi_{\text{Rabi}} = \left(\frac{g_{\text{JC}}^2}{\Delta} - \frac{g_{\text{AJC}}^2}{\Sigma} \right)$, $\chi_{\text{JC}} = \frac{g_{\text{JC}}^2}{\Delta}$, and $\chi_{\text{AJC}} = -\frac{g_{\text{AJC}}^2}{\Sigma}$ where $\Delta = \omega_q - \omega_r$ is the detuning and $\Sigma = \omega_q + \omega_r$.

These shifts produce qubit-state dependent transmission spectra. For an initial qubit state $|g\rangle$ or $|e\rangle$, the cavity resonance is displaced by $\pm \chi$. The expressions for dispersive shifts highlight an important difference between the three coupling regimes. In the JC case, the shift χ_{JC} scales inversely with the detuning Δ . In the AJC case, however, the shift χ_{AJC} involves the large frequency sum Σ , which can suppress the magnitude of the dispersive coupling. For the Rabi case, both contributions combine, yielding the more general expression in χ_{Rabi} . We note that the dispersive approximation for JC regime is valid when $g_{\text{JC}} \ll |\omega_r - \omega_q|$ while, the AJC coupling is valid whenever $g_{\text{AJC}} \ll \omega_r + \omega_q$, which holds over a broad range of frequencies.

The interplay between these two dispersive shift mechanisms is vividly captured in Fig. 4, which maps the resonator transmission for two distinct detuning regimes. In both panels, the plot shows the transmission for the qubit in its ground state $|g\rangle$ (red) and excited state $|e\rangle$ (blue), plotted against the probe frequency ω_p and the mixing

angle θ . Figure 4(a) shows the case of large negative detuning, $\omega_q \ll \omega_r$. Here, the behavior is dominated by the large magnitude of $|\Delta|$. The ground state shift $\chi(\theta)$ for the $|g\rangle$ branch evolves from a large positive value at $\theta = 0$ (pure JC, where $\chi_{\text{JC}} = g^2/\Delta > 0$ for $\Delta < 0$) to a much smaller negative value at $\theta = \pi/2$ (pure AJC, where $\chi_{\text{AJC}} = -g^2/\Sigma < 0$). A key feature is the existence of a *sweet spot* at a specific angle θ_0 where the JC and AJC contributions cancel exactly, $\chi_{\text{JC}} = -\chi_{\text{AJC}}$, resulting in a vanishing net dispersive shift. At this point, the resonator frequency becomes independent of the qubit state, rendering dispersive readout ineffective.

This behavior changes dramatically for large positive detuning, $\omega_q \gg \omega_r$, as shown in Fig. 4(b). In this regime, the detuning Δ is large and positive. Consequently, the JC contribution $\chi_{\text{JC}} = g^2/\Delta$ is now positive but small. The AJC contribution $\chi_{\text{AJC}} = -g^2/\Sigma$ remains negative and is also suppressed by the value of Σ . Crucially, in this parameter range, the two shifts have the same sign (both are negative or near-zero), and no cancellation occurs. The dispersive shift thus varies monotonically with θ without passing through zero, maintaining a finite readout contrast across the entire range.

These results demonstrate that the efficacy of dispersive readout in this tunable coupling architecture is highly dependent on the chosen operating point (θ, Δ) . The ability to null the dispersive shift, as in (a), could be useful for mitigating qubit dephasing during idle periods, while the robust shift in (b) is ideal for high-fidelity measurement. The cancellation condition is a unique feature arising from the interplay of two coupling paths and has no analogue in standard circuit QED.

Another crucial aspect of dispersive readout is the Purcell effect, which describes the qubit relaxation induced by photon leakage from the resonator [52]. The Purcell decay rates for the three regimes are given by

$$\Gamma_{\text{P}}^{\text{JC}} = \frac{\kappa g_{\text{JC}}^2}{\Delta^2 + \kappa^2 + g_{\text{JC}}^2}, \quad (8)$$

$$\Gamma_{\text{P}}^{\text{AJC}} = \frac{\kappa g_{\text{AJC}}^2}{\Sigma^2 + \kappa^2 + 2g_{\text{AJC}}^2}, \quad (9)$$

$$\Gamma_{\text{P}}^{\text{Rabi}} = \Gamma_{\text{JC}} + \Gamma_{\text{AJC}}. \quad (10)$$

A key difference lies in the energy denominators. In the JC case, the rate is determined solely by the detuning Δ , while in the AJC case the relevant scale is the large frequency sum Σ . As a consequence, the Purcell effect is strongly suppressed in the AJC regime, offering a potential route toward protecting the qubit from measurement-induced relaxation. In the Rabi case, both contributions coexist, leading to a larger decay rate.

Figure 5 compares the normalized Purcell decay rate Γ_{P}/κ for the JC and AJC regimes as a function of χ . For a given χ , the required coupling strengths are vastly different: achieving a large $\chi_{\text{JC}} \approx g_{\text{JC}}^2/\Delta$ requires a large g_{JC} , which directly increases $\Gamma_{\text{P}}^{\text{JC}}$. In contrast, achieving the same χ via the AJC interaction, $\chi_{\text{AJC}} \approx g_{\text{AJC}}^2/\Sigma$, requires a much larger coupling strength g_{AJC} because

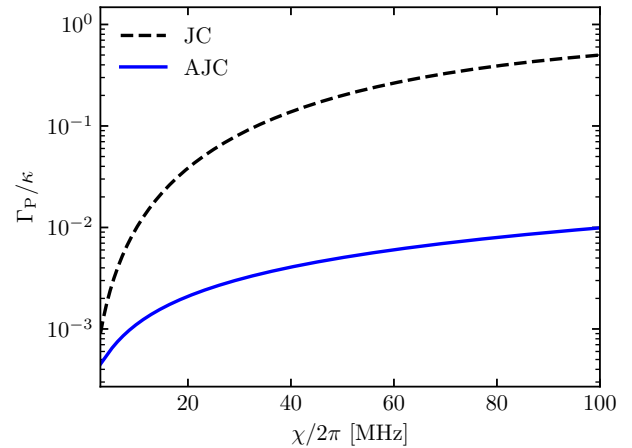


Figure 5. Comparison of the Purcell decay rate of the qubit for JC (dashed) and AJC (solid) coupling regimes. Here the qubit frequency is swiped for setting the value for χ and all other parameters are as in Fig. 2.

of the large Σ denominator. However, this large g_{AJC} does not catastrophically increase the Purcell decay, because $\Gamma_{\text{P}}^{\text{AJC}}$ is suppressed by Σ^2 . The result, as clearly shown in Fig. 5, is that for an identical dispersive shift χ , the AJC regime maintains a Purcell decay rate that is orders of magnitude lower than that of the JC regime. This demonstrates a fundamental advantage: the AJC interaction provides a pathway to achieve strong measurement contrast (large χ) while simultaneously protecting the qubit from measurement-induced relaxation (low Γ_{P}). This decoupling of the readout signal from the Purcell decay rate is a unique feature of the AJC channel and enables faster, more repeated, and more reliable qubit readout without sacrificing the qubit's coherence.

IV. PRACTICAL FEASIBILITY

The simultaneous capacitive and inductive coupling architecture described above can be implemented using standard superconducting circuit technology. Both forms of coupling have been extensively demonstrated individually in circuit QED, and their integration into a single device requires only modest extensions of current fabrication practices.

From a fabrication perspective, the capacitive coupling is straightforwardly realized by positioning a coupling pad of the qubit in close proximity to the voltage antinode of the resonator. The coupling strength g_C can be engineered by adjusting the overlap area and distance of the coupling capacitor, with values in the range of a few to tens of MHz readily achievable in transmon devices [53–55]. The inductive coupling, on the other hand, requires a shared inductive pathway or a geometrically designed mutual inductance M . This approach has been success-

fully demonstrated in flux qubits [33, 56] and fluxonium circuits [57, 58], where large magnetic dipole matrix elements enhance the strength of flux-mediated interactions. The strength g_L is tunable through the loop geometry and wire inductance, and can likewise reach values comparable to capacitive couplings in existing devices.

From a microscopic perspective, achieving simultaneous capacitive and inductive coupling requires that both transition matrix elements $\langle g|\hat{n}|e\rangle$ and $\langle g|\hat{\phi}|e\rangle$ be sufficiently nonzero. These quantities measure the charge and flux participation of the qubit transition, respectively, and both are naturally finite in transmon, flux, and fluxonium qubits for suitable external biases [53, 57, 59], ensuring that both coupling mechanisms can coexist within realistic circuit parameters.

A key practical advantage of the proposed setup is that the relative ratio g_C/g_L is determined primarily at the design stage. Thus, one can statically tailor the interaction channel (JC- or AJC-dominant) through lithographic parameters without the need for dynamical control. This removes the necessity of microwave modulation schemes that are otherwise required to access counter-rotating processes [33, 60]. The energy scales of the system also remain compatible with standard circuit QED practice. For example, assuming a resonator frequency $\omega_r/2\pi \sim 5$ GHz and a qubit frequency $\omega_q/2\pi \sim 4\text{--}7$ GHz, coupling strengths $g_C, g_L/2\pi \sim 50\text{--}150$ MHz are realistic. In this range, the effective JC or AJC couplings g_{JC}, g_{AJC} are large enough to produce observable transmission signatures while still well below the frequencies Δ, Σ , ensuring the dispersive approximation remains valid in typical regimes. The suppression of the Purcell effect in the AJC configuration, as highlighted above, further enhances qubit coherence, which is advantageous for readout fidelity [52].

Another important consideration is the effect of circuit asymmetries and fabrication tolerances. Small mismatches between the intended g_C and g_L values will generically lead to an anisotropic Rabi Hamiltonian with both JC and AJC contributions. However, this does not eliminate the unique features of the proposed architecture, since the relative strengths of the two channels can still be tuned over a broad range. Moreover, post-fabrication fine-tuning of the couplings may be achievable using tunable inductive elements (such as SQUID loops) [4, 61] or by varying the qubit bias point, providing additional flexibility.

V. CONCLUSIONS

In this work, we have proposed and analyzed a circuit QED architecture that enables static, on-demand control over the fundamental channels of light-matter interaction. By simultaneously coupling a superconducting qubit to both the voltage and current antinodes of a coplanar waveguide resonator, our scheme naturally realizes the ARM with tunable relative strength between

JC and AJC interactions. The key innovation is to engineer the interference between capacitive and inductive coupling paths via circuit design.

We have demonstrated that this approach provides several significant advantages over conventional circuit QED implementations. First, it enables access to pure JC and pure AJC interaction Hamiltonians without relying on the RWA or external parametric modulation. Second, it offers unprecedented control over dispersive readout properties, including the ability to completely cancel the dispersive shift at specific operating points—a feature with no analogue in standard architectures. Third, the AJC regime provides a unique pathway to achieve strong measurement contrast while simultaneously suppressing Purcell decay, effectively decoupling readout sensitivity from qubit relaxation.

We note that alternative approaches to realize anisotropic or blue-sideband (AJC-like) interactions have relied on periodic modulation of system parameters, such as qubit frequency or coupling strengths [8, 39, 41, 42, 62]. By contrast, the architecture presented here engineers the anisotropy *statically* at the circuit level via the coherent interference of capacitive and inductive coupling paths; no external modulation tones are required. This static approach reduces control-channel complexity and avoids modulation-induced heating or ancillary drive errors, while offering an immediately implementable device-level knob for the ARM parameter space.

The proposed architecture is readily implementable with current superconducting circuit technology and compatible with various qubit platforms, including transmons, flux qubits, and fluxoniums. The coupling ratio g_C/g_L is primarily determined during device design through lithographic patterning, making the interaction type a static property that requires no dynamic control. This simplicity, combined with the rich physics accessible through continuous tuning of the mixing angle θ , makes the platform particularly versatile for exploring quantum phenomena across the full parameter space of the ARM.

Looking forward, this work opens several promising directions for future research. The clean isolation of AJC interactions could enable novel quantum information protocols leveraging two-photon processes and squeezed states. The ability to statically control interaction symmetries may facilitate the exploration of symmetry-protected quantum phases and critical phenomena. Furthermore, the enhanced readout capabilities demonstrated here could be integrated with quantum error correction schemes to improve fault-tolerant quantum computing architectures. We anticipate that this geometrically engineered coupling approach will provide a valuable new toolset for fundamental studies of light-matter interactions and the development of advanced quantum technologies.

Appendix A: Circuit Hamiltonian derivation

In this Appendix we provide the derivation of the effective qubit—resonator Hamiltonian given in the text. We start from deriving the Lagrangian of the circuit diagram shown in Fig. 1. The resonator is implemented as a CPW, which can be modeled as a distributed transmission line characterized by inductance per unit length L' and capacitance per unit length C' [63]. The effective values of L' and C' are dictated by the geometry of the center conductor and ground planes of the CPW, as well as the dielectric properties of the substrate. These quantities can be estimated using conformal mapping techniques [64] or electromagnetic field solvers. The resonant frequency of such a structure is determined by the boundary conditions and the propagation characteristics of electromagnetic waves in the waveguide. For typical superconducting CPW resonators fabricated on silicon or sapphire substrates, L' and C' typically fall in the range of a few hundred nH/m and a few hundred pF/m, respectively, leading to phase velocities on the order of $v_p \sim 10^8$ m/s and resonance frequencies in the microwave regime ($\omega_r/2\pi \sim 5-10$ GHz) for physical lengths $\ell \sim 1$ cm.

Let us consider a resonator of length ℓ and open boundary conditions at both ends (a $\lambda/2$ resonator). The Lagrangian of the uncoupled CPW resonator is given by

$$\mathcal{L}_{\text{res}} = \int_{-\ell/2}^{+\ell/2} dx \left[\frac{C'}{2} (\partial_t \Phi(x, t))^2 - \frac{1}{2L'} (\partial_x \Phi(x, t))^2 \right], \quad (\text{A1})$$

with boundary conditions imposed by the assumption of open-circuit terminations at both ends: $\partial_x \Phi(\pm \ell/2, t) = 0$, which corresponds to vanishing current $I(\pm \ell/2, t) = \frac{1}{L'} \partial_x \Phi(\pm \ell/2, t)$ at the endpoints. To quantize the system, we first perform a mode decomposition of the resonator field in terms of the eigenmodes $f_n(x)$ as

$$\Phi(x, t) = \sum_{n=0}^{\infty} \phi_n(t) f_n(x), \quad (\text{A2})$$

where $\phi_n(t)$ is the generalized coordinate of the n -th mode. Due to the boundary conditions, $\partial_x f_n(\pm \ell/2) = 0$, the eigenmodes of the resonator take the form

$$f_n(x) = \begin{cases} \sqrt{\frac{2}{\ell}} \sin\left(\frac{n\pi x}{\ell}\right), & n = 1, 3, \dots \\ \sqrt{\frac{2}{\ell}} \cos\left(\frac{n\pi x}{\ell}\right), & n = 2, 4 \dots \end{cases} \quad (\text{A3})$$

Substituting this expansion into the Lagrangian and integrating over x , we obtain the mode Lagrangian for the resonator

$$\mathcal{L}_{\text{res}} = \sum_n \left[\frac{1}{2} C' \dot{\phi}_n^2 - \frac{1}{2} \frac{1}{L'} k_n^2 \phi_n^2 \right], \quad (\text{A4})$$

with $k_n = n\pi/\ell$, for $n \geq 1$. The corresponding angular frequency of the n -th mode is given by $\omega_n = v_p k_n$, where

$v_p = 1/\sqrt{L' C'}$ is the phase velocity in the resonator. In the following, we consider the effective coupling of the qubit to a single mode ($n = r$) of the resonator. Thus we can easily assume $\Phi(x, t) = \phi_r(t) f_r(x)$.

The qubit's degree of freedom is described by the node flux variable $\phi_q(t)$. The qubit has a Lagrangian of the form

$$\mathcal{L}_{\text{qubit}} = \frac{C_q}{2} \dot{\phi}_q^2 - \frac{1}{2L_q} \phi_q^2 + E_J \cos\left(\frac{2\pi}{\Phi_0} \phi_q - \Phi_{\text{ext}}\right), \quad (\text{A5})$$

where C_q is the intrinsic qubit capacitance, L_q is the shunting inductance, E_J is the Josephson energy and Φ_{ext} is the external flux through the qubit circuit.

The capacitive coupling between the qubit and the resonator at point x_C contributes an interaction term

$$\begin{aligned} \mathcal{L}_C &= \frac{C_g}{2} \left(\dot{\phi}_q - \partial_t \Phi(x_C, t) \right)^2 \\ &= \frac{C_g}{2} \left(\dot{\phi}_q - \dot{\phi}_r f_r(x_C) \right)^2, \end{aligned} \quad (\text{A6})$$

The inductive coupling at point x_M is also modeled by a term

$$\begin{aligned} \mathcal{L}_M &= \frac{M}{L_0} I_c \sin\left(\frac{2\pi}{\Phi_0} \phi_q\right) \partial_x \Phi(x_M, t) \\ &= \frac{M}{L_0} I_c \sin\left(\frac{2\pi}{\Phi_0} \phi_q\right) \phi_r \partial_x f_r(x_M). \end{aligned} \quad (\text{A7})$$

From the total Lagrangian $\mathcal{L} = \mathcal{L}_{\text{res}} + \mathcal{L}_{\text{qubit}} + \mathcal{L}_C + \mathcal{L}_M$, we obtain the canonical momenta

$$Q_r = \frac{\partial \mathcal{L}}{\partial \dot{\phi}_r} = C_0 \dot{\phi}_r - C_g \left(\dot{\phi}_q - \dot{\phi}_r f_r(x_C) \right) f_r(x_C), \quad (\text{A8})$$

$$Q_q = \frac{\partial \mathcal{L}}{\partial \dot{\phi}_q} = C_{\Sigma} \dot{\phi}_q - C_g \dot{\phi}_r f_r(x_C). \quad (\text{A9})$$

where, $C_{\Sigma} = C_g + C_q$. Now, the Legendre transform $\mathcal{H} = Q_r \dot{\phi}_r + Q_q \dot{\phi}_q - \mathcal{L}$ gives the Hamiltonian

$$\begin{aligned} \mathcal{H} &= 4E_{C,r} n_r^2 + E_{L,r} k_r^2 \phi_r^2 + 4E_{C,q} n_q^2 + E_{L,q} \phi_q^2 \\ &\quad - E_J \cos\left(\frac{2\pi}{\Phi_0} \phi_q - \Phi_{\text{ext}}\right) + 8E_{C,qr} f_r(x_C) n_q n_r \\ &\quad - \frac{M}{L_0} \partial_x f_r(x_M) I_c \sin\left(\frac{2\pi}{\Phi_0} \phi_q\right) \phi_r, \end{aligned} \quad (\text{A10})$$

where we used the charge operators $n_i = Q_i/2e$, $E_{L,r} = \frac{1}{2L_0}$, $E_{L,q} = \frac{1}{2L_q}$ and the capacitive energy coefficients $E_{C,i}$ are given by

$$E_{C,q} = \frac{e^2}{2} \frac{f(x_C)^4 C_g^2 C_q + 2C_0 f(x_C)^2 C_g C_{\Sigma} + C_0^2 C_{\Sigma}}{(f(x_C)^2 C_g C_q + C_0 C_{\Sigma})^2}, \quad (\text{A11})$$

$$E_{C,r} = \frac{e^2}{2} \frac{C_{\Sigma} (f(x_C)^2 C_g C_q + 2C_0 C_{\Sigma})}{2 (f(x_C)^2 C_g C_q + C_0 C_{\Sigma})^2}, \quad (\text{A12})$$

$$E_{C,qr} = \frac{e^2}{2} \frac{C_g (f(x_C)^2 C_g C_q + 2C_0 C_{\Sigma})}{(f(x_C)^2 C_g C_q + C_0 C_{\Sigma})^2}. \quad (\text{A13})$$

Now, we quantize the resonator and qubit modes by promoting the circuit variables to operators and introducing bosonic annihilation (creation) operators $\hat{a}(\hat{a}^\dagger)$ and $\hat{b}(\hat{b}^\dagger)$ for the resonator and qubit modes, respectively. The canonical quantization is performed using

$$\hat{\phi}_r = \left(\frac{\hbar^2 E_{C,r}}{k_r^2 E_{L,r}} \right)^{1/4} (\hat{a} + \hat{a}^\dagger), \quad (\text{A14})$$

$$\hat{n}_r = i \left(\frac{\hbar^2 k_r^2 E_{L,r}}{16 E_{C,r}} \right)^{1/4} (\hat{a}^\dagger - \hat{a}), \quad (\text{A15})$$

$$\hat{\phi}_q = \left(\frac{\hbar^2 E_{C,q}}{E_{L,q}} \right)^{1/4} (\hat{b} + \hat{b}^\dagger), \quad (\text{A16})$$

$$\hat{n}_q = i \left(\frac{\hbar^2 E_{L,q}}{16 E_{C,q}} \right)^{1/4} (\hat{b}^\dagger - \hat{b}). \quad (\text{A17})$$

The final expression for the total Hamiltonian is given by

$$\mathcal{H} = \hbar \omega_r \left(\hat{a}^\dagger \hat{a} + \frac{1}{2} \right) + \hbar \omega_q \left(\hat{b}^\dagger \hat{b} + \frac{1}{2} \right) - g_C (\hat{b}^\dagger - \hat{b}) (\hat{a}^\dagger - \hat{a}) - g_L (\hat{b} + \hat{b}^\dagger) (\hat{a} + \hat{a}^\dagger), \quad (\text{A18})$$

with the mode frequencies

$$\omega_r = 4k_r \sqrt{E_{C,r} E_{L,r}}, \quad (\text{A19})$$

$$\omega_q = 4 \sqrt{E_{C,q} \left(E_{L,q} + \left(\frac{2\pi}{\Phi_0} \right)^2 \frac{E_J}{2} \right)}, \quad (\text{A20})$$

and coupling constants

$$g_C = 8\hbar E_{C,q} f_r(x_C) \times \left(\frac{\left(E_{L,q} + \left(\frac{2\pi}{\Phi_0} \right)^2 \frac{E_J}{2} \right) k_r^2 E_{L,r}}{16 E_{C,q}} \right)^{1/4}, \quad (\text{A21})$$

$$g_L = \hbar M \frac{2\pi}{\Phi_0} I_c \frac{\partial_x f_r(x_M)}{L_0} \times \left(\frac{E_{C,r}}{k_r^2 E_{L,r}} \frac{E_{C,q}}{\left(E_{L,q} + \left(\frac{2\pi}{\Phi_0} \right)^2 \frac{E_J}{2} \right)} \right)^{1/4}. \quad (\text{A22})$$

Let us assume the qubit is effectively coupled to the fundamental mode ($r = 1$) of the resonator, so that we have $f_r(x) = \sqrt{2/\ell} \sin(\pi x/\ell)$. The inductive coupling g_L is maximum when $x_M = 0$, corresponding to the current antinode. Conversely, the capacitive coupling g_C changes sign depending on whether the qubit is connected at $x_C = -\ell/2$ or $x_C = +\ell/2$, corresponding to voltage antinodes of opposite polarity. This completes the derivation of the effective Hamiltonian for simultaneous capacitive and inductive qubit-resonator coupling.

[1] A. Blais, A. L. Grimsme, S. M. Girvin, and A. Wallraff, Rev. Mod. Phys. **93**, 025005 (2021).

[2] R. J. Schoelkopf and S. M. Girvin, Nature **451**, 664 (2008).

[3] A. Wallraff, D. I. Schuster, A. Blais, L. Frunzio, R.-S. Huang, J. Majer, S. Kumar, S. M. Girvin, and R. J. Schoelkopf, Nature **431**, 162 (2004).

[4] A. Blais, R.-S. Huang, A. Wallraff, S. M. Girvin, and R. J. Schoelkopf, Physical Review A **69**, 062320 (2004).

[5] I. I. Rabi, Physical Review **51**, 652 (1937).

[6] E. Jaynes and F. Cummings, Proceedings of the IEEE **51**, 89 (1963).

[7] M. Hofheinz, E. M. Weig, M. Ansmann, R. C. Bialczak, E. Lucero, M. Neeley, A. D. O'Connell, H. Wang, J. M. Martinis, and A. N. Cleland, Nature **454**, 310 (2008).

[8] F. Deppe, M. Mariantoni, E. P. Menzel, A. Marx, S. Saito, K. Kakuyanagi, H. Tanaka, T. Meno, K. Semba, H. Takayanagi, E. Solano, and R. Gross, Nature Physics **4**, 686 (2008).

[9] J. Majer, J. M. Chow, J. M. Gambetta, J. Koch, B. R. Johnson, J. A. Schreier, L. Frunzio, D. I. Schuster, A. A. Houck, A. Wallraff, A. Blais, M. H. Devoret, S. M. Girvin, and R. J. Schoelkopf, Nature **449**, 443 (2007).

[10] M. A. Sillanpää, J. I. Park, and R. W. Simmonds, Nature **449**, 438 (2007).

[11] T. Niemczyk, F. Deppe, H. Huebl, E. P. Menzel, F. Hocke, M. J. Schwarz, J. J. Garcia-Ripoll, D. Zueco, T. Hümmer, E. Solano, A. Marx, and R. Gross, Nature Physics **6**, 772 (2010).

[12] J. Casanova, G. Romero, I. Lizuain, J. J. García-Ripoll, and E. Solano, Physical Review Letters **105**, 263603 (2010).

[13] E. K. Twyeffort Irish, Physical Review Letters **99**, 173601 (2007).

[14] D. Zueco, G. M. Reuther, S. Kohler, and P. Hänggi, Physical Review A **80**, 033846 (2009).

[15] F. Bloch and A. Siegert, Physical Review **57**, 522 (1940).

[16] J. Tuorila, M. Silveri, M. Sillanpää, E. Thuneberg, Y. Makhlin, and P. Hakonen, Physical Review Letters **105**, 257003 (2010).

[17] P. Forn-Díaz, J. Lisenfeld, D. Marcos, J. J. García-Ripoll, E. Solano, C. J. P. M. Harmans, and J. E. Mooij, Physical Review Letters **105**, 237001 (2010).

[18] E. Solano, G. S. Agarwal, and H. Walther, Physical Review Letters **90**, 027903 (2003).

[19] F. Beaudoin, J. M. Gambetta, and A. Blais, Phys. Rev. A **84**, 043832 (2011).

[20] K. K. W. Ma and C. K. Law, Physical Review A **92**, 023842 (2015).

[21] A. Ridolfo, M. Leib, S. Savasta, and M. J. Hartmann, Physical Review Letters **109**, 193602 (2012).

[22] M.-J. Hwang, R. Puebla, and M. B. Plenio, Physical Review Letters **109**, 193603 (2012).

view Letters **115**, 180404 (2015).

[23] M.-J. Hwang, M. Kim, and M.-S. Choi, Physical Review Letters **116**, 153601 (2016).

[24] A. Le Boit  , M.-J. Hwang, H. Nha, and M. B. Plenio, Physical Review A **94**, 033827 (2016).

[25] H. Zheng, S. Y. Zhu, and M. S. Zubairy, Phys. Rev. Lett. **101**, 200404 (2008).

[26] Z. Ficek and R. Tana  , Physics Reports **372**, 369 (2002).

[27] J. Jing, Z.-G. L  , and Z. Ficek, Physical Review A **79**, 044305 (2009).

[28] Z. L   and H. Zheng, Physical Review A **86**, 023831 (2012).

[29] A. L. Grimsmo and S. Parkins, Phys. Rev. A **87**, 033814 (2013).

[30] S. Ashhab, J. R. Johansson, A. M. Zagoskin, and F. Nori, Phys. Rev. A **75**, 063414 (2007).

[31] D. Ballester, G. Romero, J. J. Garc  a-Ripoll, F. Deppe, and E. Solano, Physical Review X **2**, 021007 (2012).

[32] C. Deng, J.-L. Orgiazzi, F. Shen, S. Ashhab, and A. Lupascu, Physical Review Letters **115**, 133601 (2015).

[33] F. Yoshihara, T. Fuse, S. Ashhab, K. Kakuyanagi, S. Saito, and K. Semba, Nature Physics **13**, 44 (2017).

[34] Y.-H. Chen, A. Miranowicz, X. Chen, Y. Xia, and F. Nori, Phys. Rev. Appl. **18**, 064059 (2022).

[35] F. Beaudoin, M. P. da Silva, Z. Dutton, and A. Blais, Physical Review A **86**, 022305 (2012).

[36] J. D. Strand, M. Ware, F. Beaudoin, T. A. Ohki, B. R. Johnson, A. Blais, and B. L. T. Plourde, Physical Review B **87**, 220505 (2013).

[37] G. Wang, R. Xiao, H. Shen, C. Sun, and K. Xue, Scientific reports **9**, 4569 (2019).

[38] A. Wallraff, D. I. Schuster, A. Blais, J. M. Gambetta, J. Schreier, L. Frunzio, M. H. Devoret, S. M. Girvin, and R. J. Schoelkopf, Phys. Rev. Lett. **99**, 050501 (2007).

[39] P. J. Leek, S. Filipp, P. Maurer, M. Baur, R. Bianchetti, J. M. Fink, M. G  ppl, L. Steffen, and A. Wallraff, Phys. Rev. B **79**, 180511 (2009).

[40] S. Novikov, T. Sweeney, J. E. Robinson, S. P. Premaratne, B. Suri, F. C. Wellstood, and B. S. Palmer, Nature Physics **12**, 75 (2015).

[41] Y. Lu, S. Chakram, N. Leung, N. Earnest, R. K. Naik, Z. Huang, P. Groszkowski, E. Kapit, J. Koch, and D. I. Schuster, Phys. Rev. Lett. **119**, 150502 (2017).

[42] A. V. Dodonov, A. Napoli, and B. Militello, Physical Review A **99**, 033823 (2019).

[43] X. Wang, A. Miranowicz, H.-R. Li, and F. Nori, Phys. Rev. A **96**, 063820 (2017).

[44] C. Mayero and J. A. Omolo, Quantum Information Processing **23**, 10.1007/s11128-024-04390-1 (2024).

[45] B. M. Rodr  guez-Lara, H. Moya-Cessa, and A. B. Klimov, Phys. Rev. A **71**, 023811 (2005).

[46] A. Baksic and C. Ciuti, Physical Review Letters **112**, 173601 (2014).

[47] Q.-T. Xie, S. Cui, J.-P. Cao, L. Amico, and H. Fan, Phys. Rev. X **4**, 021046 (2014).

[48] A. Frisk Kockum, A. Miranowicz, S. De Liberato, S. Savasta, and F. Nori, Nature Reviews Physics **1**, 19 (2019).

[49] A. Blais, J. Gambetta, A. Wallraff, D. I. Schuster, S. M. Girvin, M. H. Devoret, and R. J. Schoelkopf, Phys. Rev. A **75**, 032329 (2007).

[50] J. Fink, M. G  ppl, M. Baur, R. Bianchetti, P. J. Leek, A. Blais, and A. Wallraff, Nature **454**, 315 (2008).

[51] L. S. Bishop, J. Chow, J. Koch, A. Houck, M. Devoret, E. Thuneberg, S. Girvin, and R. Schoelkopf, Nature Physics **5**, 105 (2009).

[52] E. A. Sete, J. M. Gambetta, and A. N. Korotkov, Phys. Rev. B **89**, 104516 (2014).

[53] J. Koch, T. M. Yu, J. Gambetta, A. A. Houck, D. I. Schuster, J. Majer, A. Blais, M. H. Devoret, S. M. Girvin, and R. J. Schoelkopf, Physical Review A **76**, 042319 (2007).

[54] J. A. Schreier, A. A. Houck, J. Koch, D. I. Schuster, B. R. Johnson, J. M. Chow, J. M. Gambetta, J. Majer, L. Frunzio, M. H. Devoret, S. M. Girvin, and R. J. Schoelkopf, Physical Review B **77**, 180502 (2008).

[55] H. Paik, D. I. Schuster, L. S. Bishop, G. Kirchmair, G. Catelani, A. P. Sears, B. R. Johnson, M. J. Reagor, L. Frunzio, L. I. Glazman, S. M. Girvin, M. H. Devoret, and R. J. Schoelkopf, Physical Review Letters **107**, 240501 (2011).

[56] A. Wallraff, D. I. Schuster, A. Blais, L. Frunzio, J. Majer, M. H. Devoret, S. M. Girvin, and R. J. Schoelkopf, Physical Review Letters **95**, 060501 (2005).

[57] V. E. Manucharyan, J. Koch, L. I. Glazman, and M. H. Devoret, Science **326**, 113 (2009).

[58] L. B. Nguyen, Y.-H. Lin, A. Somoroff, R. Mencia, N. Grabon, and V. E. Manucharyan, Phys. Rev. X **9**, 041041 (2019).

[59] F. Bao, H. Deng, D. Ding, R. Gao, X. Gao, C. Huang, X. Jiang, H.-S. Ku, Z. Li, X. Ma, X. Ni, J. Qin, Z. Song, H. Sun, C. Tang, T. Wang, F. Wu, T. Xia, W. Yu, F. Zhang, G. Zhang, X. Zhang, J. Zhou, X. Zhu, Y. Shi, J. Chen, H.-H. Zhao, and C. Deng, Phys. Rev. Lett. **129**, 010502 (2022).

[60] P. Forn-D  az, C. Warren, C. Chang, A. Vadiraj, and C. Wilson, Physical Review Applied **8**, 054015 (2017).

[61] V. E. Manucharyan, N. A. Masluk, A. Kamal, J. Koch, L. I. Glazman, and M. H. Devoret, Phys. Rev. B **85**, 024521 (2012).

[62] Y. Yan, Z. L  , J. Luo, and H. Zheng, Phys. Rev. A **96**, 033802 (2017).

[63] D. M. Pozar, *Microwave engineering: theory and techniques* (John Wiley & Sons, 2021).

[64] C. P. Wen, IEEE Transactions on Microwave Theory and Techniques **17**, 1087 (2003).